星形成ゼミ

#339 1-8 担当：片岡

1. Particle acceleration and magnetic field amplification in massive young stellar object jets

Anabella Araudo, Marco Padovani, Alexandre Marcowith

2. A VLA Census of the Galactic H II Region Population

William P. Armentrout, Loren D. Anderson, Trey V. Wenger, Dana S. Balser, Thomas M. Bania ⋆

3. ALMA-IRDC: Dense gas mass distribution from cloud to core scales

A. T. Barnes, J. D. Henshaw, F. Fontani, J. E. Pineda, G. Cosentino, J. C. Tan, P. Caselli, I. Jiménez-Serra, C. Y. Law, A. Avison, F. Bigiel, S. Feng, S. Kong, S. N. Longmore, L. Moser, R. J. Parker, Á. Sánchez-Monge, K. Wang

4. Fragmentation in the massive G31.41+0.31 protocluster

M. T. Beltrán, V. M. Rivilla, R. Cesaroni, L. T. Maud, D. Galli, L. Moscadelli, A. Lorenzani, A. Ahmadi, H. Beuther, T. Csengeri, S. Etoka, C. Goddi, P. D. Klaassen, R. Kuiper, M. S. N. Kumar, T. Peters, Á. Sánchez-Monge, P. Schilke, F. van der Tak, S. Vig, H. Zinnecker

5. Fitting an Analytic Magnetic Field to a Prestellar Core

Gianfranco Bino, Shantanu Basu

6. Self-scattering on large, porous grains in protoplanetary disks with dust settling

Robert Brunngräber, Sebastian Wolf

7. Magnetic fields and Star Formation around HII regions: The S235 complex

R. Devaraj, D. P. Clemens, L. K. Dewangan, A. Luna, T. P. Ray, J. Mackey

8. Water in star-forming regions (WISH): Physics and chemistry from clouds to disks as probed by Herschel spectroscopy

E. F. van Dishoeck, L. E. Kristensen, the WISH team

Self-scattering on large, porous grains in protoplanetary disks with dust settling

Robert Brunngräber, Sebastian Wolf

Observations of protoplanetary disks (PPDs) at sub-mm wavelengths suggest that polarisation is caused by scattering of thermal radiation. Most of the dust models that are used to explain these observations have major drawbacks: They either use much smaller grains than expected from dust evolution models, or result in lower polarisations than observed. We investigate the effect of dust grain porosity on the polarisation due to scattering at sub-mm wavelengths arising from grains of up to mm sizes, as they are expected to be present in the midplane of PPDs. Using the effective medium theory, we calculated the optical properties of porous dust and used them to predict the behaviour of the scattering polarisation. Subsequently, radiative transfer simulations for PPDs with porous dust were performed to analyse the additional effect of the optical depth structure, and thus the effect of multiple scattering events and inhomogeneous temperature distributions on the polarisation. We find that porous dust with moderate filling factors of about 10\% increase the polarisation compared to compact grains. For higher grain porosities, that is, grains with a filling factor of 1\% or lower, the extinction opacity decreases, as does the optical depth of a disk with constant mass. Consequently, the unpolarised direct radiation dominates the scattered flux, and the polarisation drops rapidly. Even though the simulated polarisation is higher than in the case of compact grains, it is still below the typical observed values for face-on disks. However, the polarisation can be increased when crucial model assumptions derived from disk and dust evolution theories, for instance, dust settling and mm-sized dust grains, are dropped. In the case of inclined disks, however, our reference model is able to achieve polarisation degrees of about 1\%, and using higher disk masses, even higher than this.

arXiv:2103.04819 **[astro-ph.SR]**

- **原始惑星系円盤の偏光は散乱による事がわかっている。**
- **ダストの空隙率の影響を調べた。**
- **空隙がある方が偏光度が上がる場合があることがわかった。**

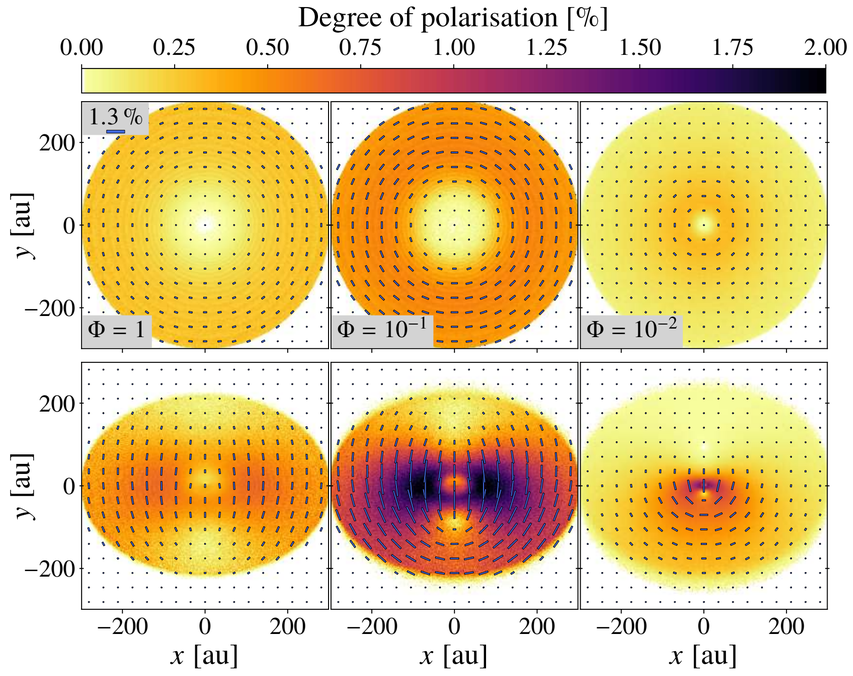

Fig. 8. Same as Fig. 7, but for a disk with a ten times higher dust mass The lengths of the polarisation vectors are scaled to the polarisatior degree, as indicated in the top left corner.

Millimeter polarization

- before ALMA -

HD 163296

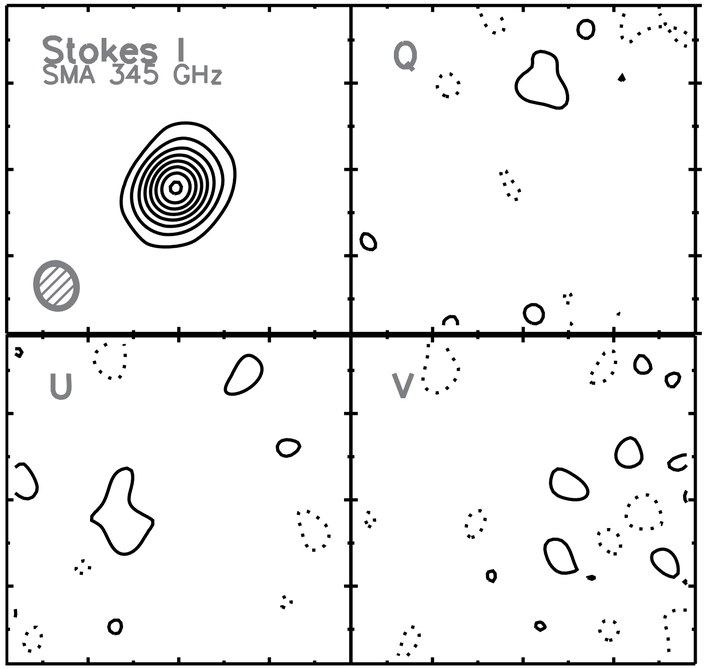

Hughes et al. 2009

upper limit ~ 1 %

Non-detection on HD 163296, TW Hya. GM Aur and DG Tau (Hughes et al. 2009, 2013). 2 sigma detection on HL Tau (Stephens et al. 2014)

ALMA polarization (Class II disks)

HD 142527

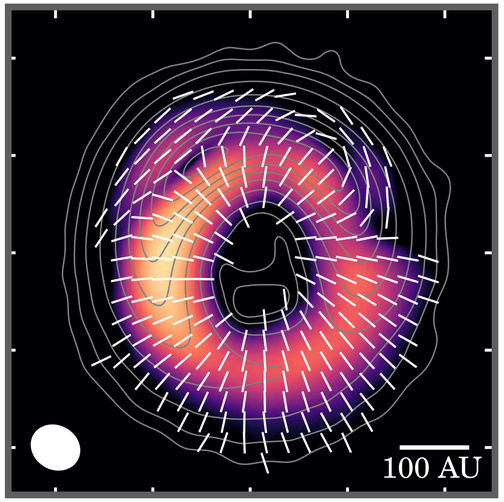

IM Lup

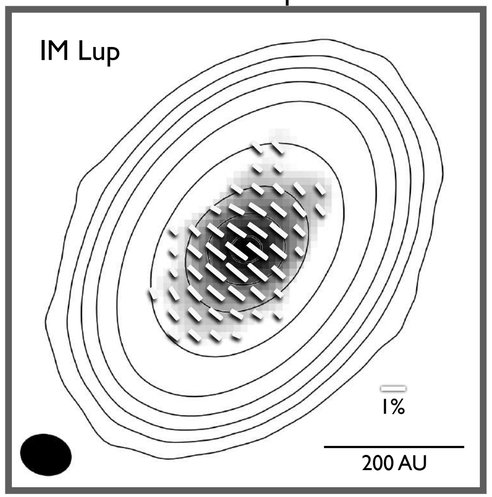

CW Tau

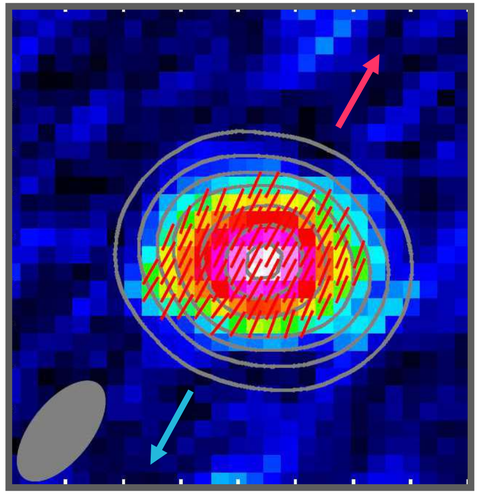

HL Tau

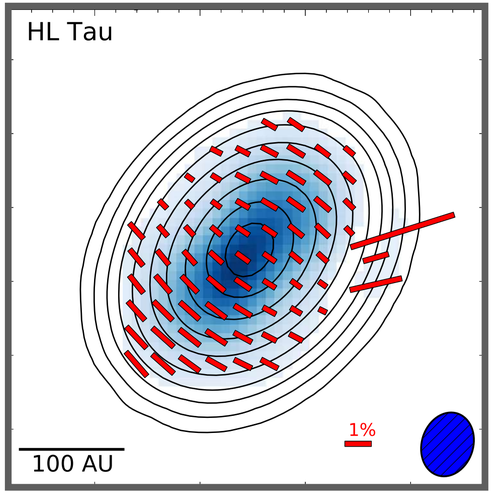

HD 163296

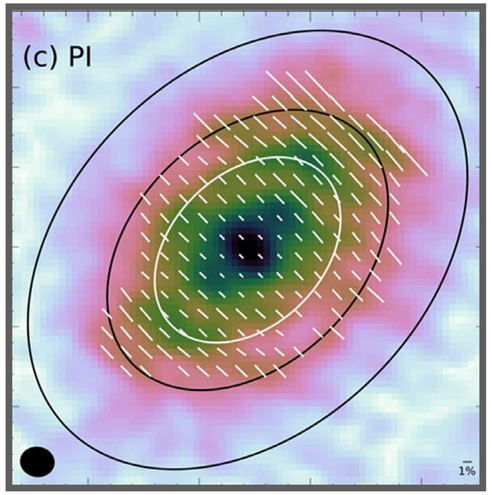

DG Tau

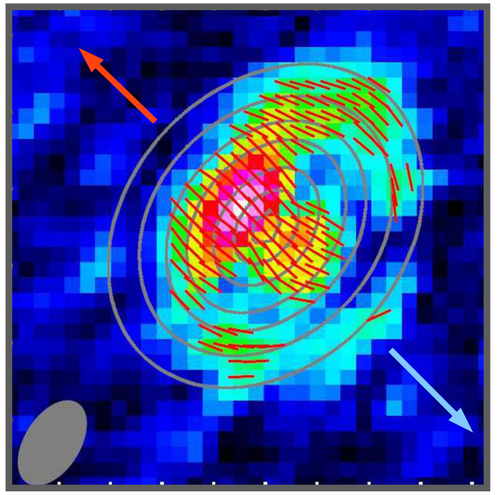

Kataoka et al. 2016, Hull et al. 2018, Bacciotti et al. 2018, Dent et al. 2019, Stephens et al. 2017, cf. Kataoka et al. 2017, Ohashi et al. 2018

what can we learn from self-scattering?

Assumption: spherical dust grains

Albedo = efficiency of scattering

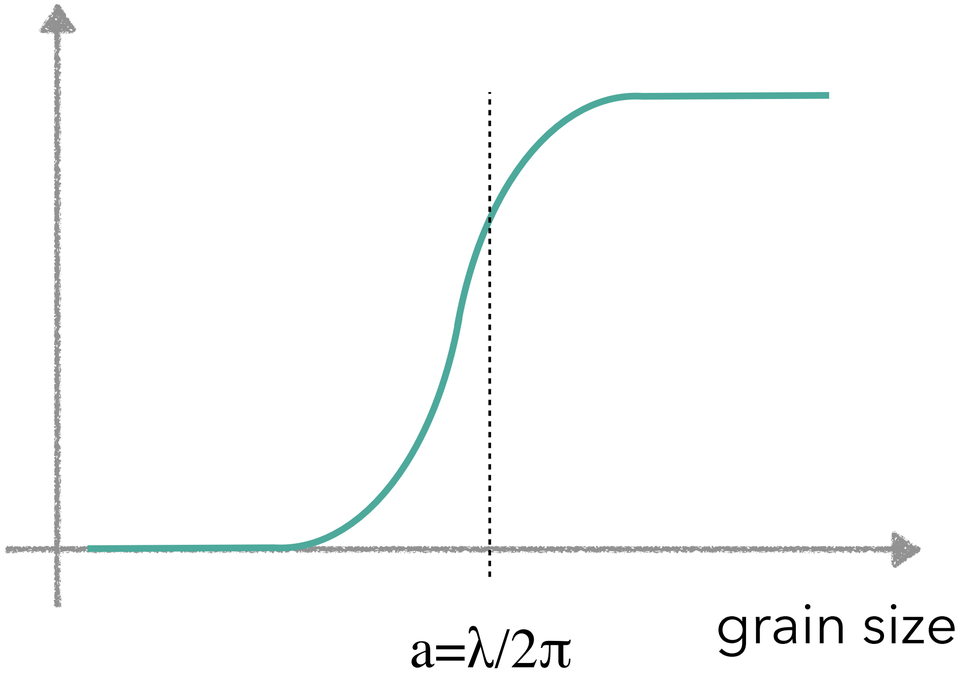

Polarization at single scattering

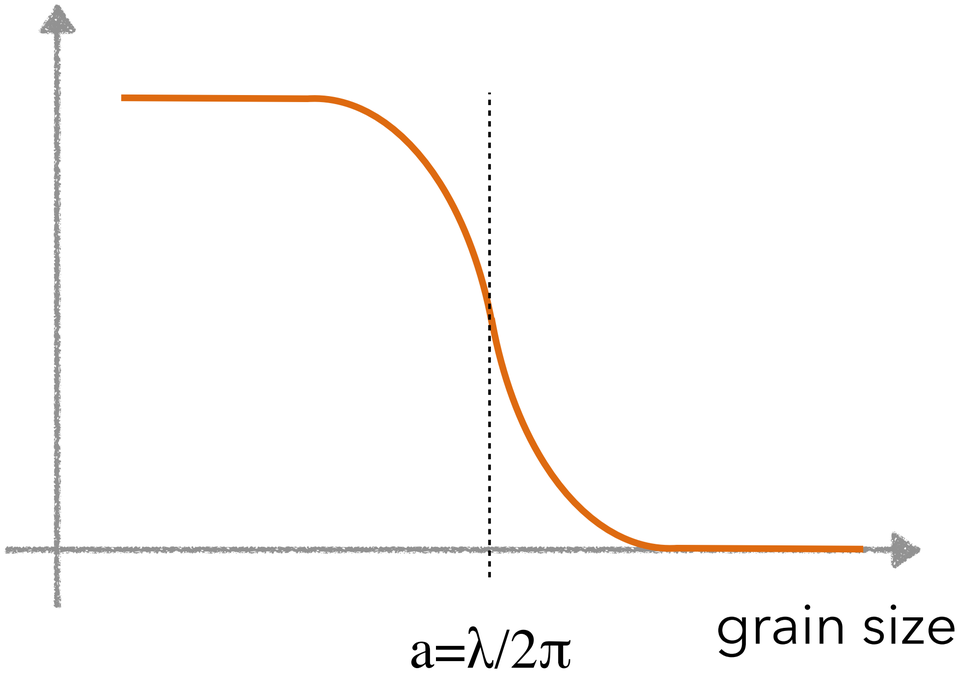

Scattering-induced polarization is detectable only when a=λ/2π

what can we learn from self-scattering?

Anisotropies of radiation field at the observed wavelengths.

× **Grain size** = **Polarization**

Prediction of polarization fraction

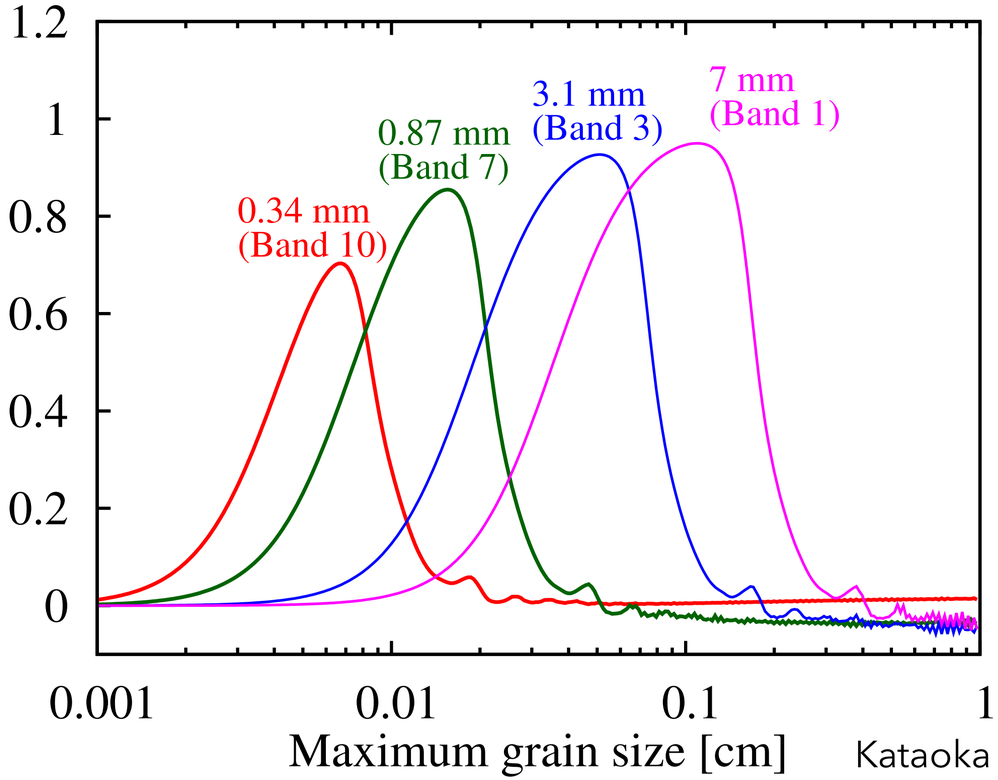

Kataoka et al., 2015

(grain size) ~ λ/2π

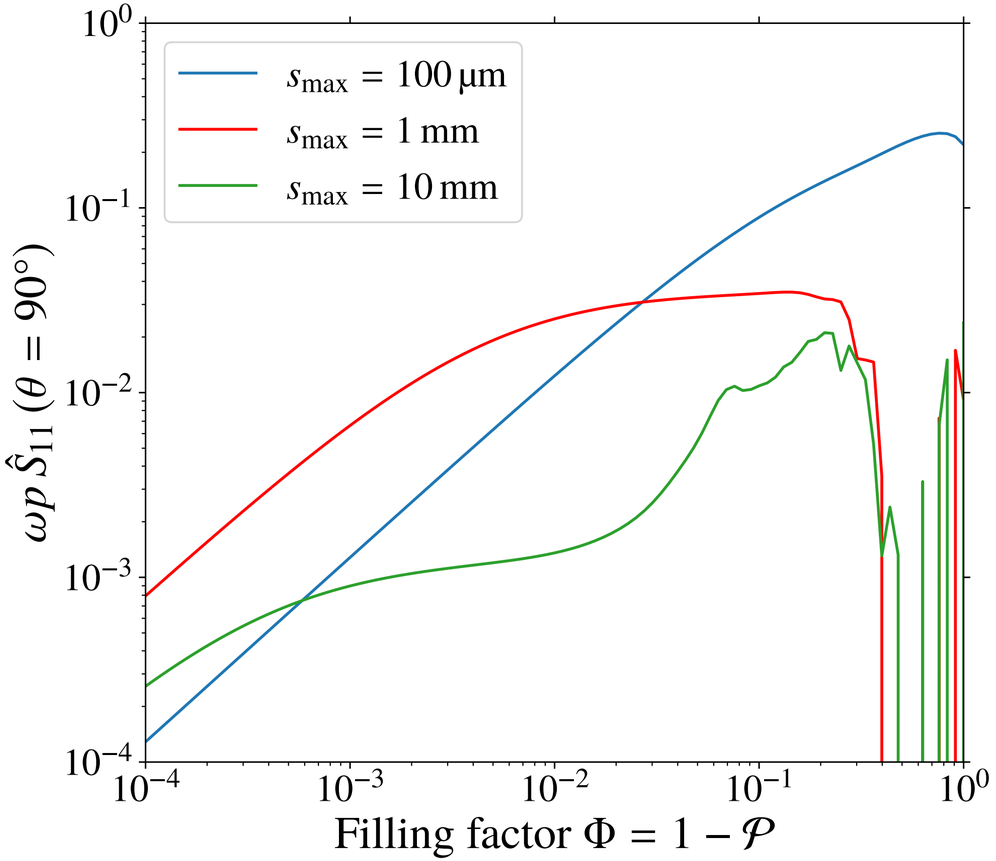

Fig. 2. Product of albedo ω, single-scattering polarisation p, and probability density function $\hat{S}_{11}$ for the scattering angle $\theta = 90°$. All quantities are calculated for a grain size distribution with $q = -3.5$, $s_{\min} = 5\,\text{nm}$ and three different maximum grain sizes $s_{\max} = 100\,\mu\text{m}$ (*blue*), 1 mm (*red*), and 10 mm (*green*) at a wavelength of 850 µm for astrosil; see Sect. 2.3 for the corresponding discussion.

- アルベドとpとS11をかけたものがだいたいの偏光の効率を表している。
- 1mmとか 1cmダストでは、充填率10%くらいだと偏光度が高い

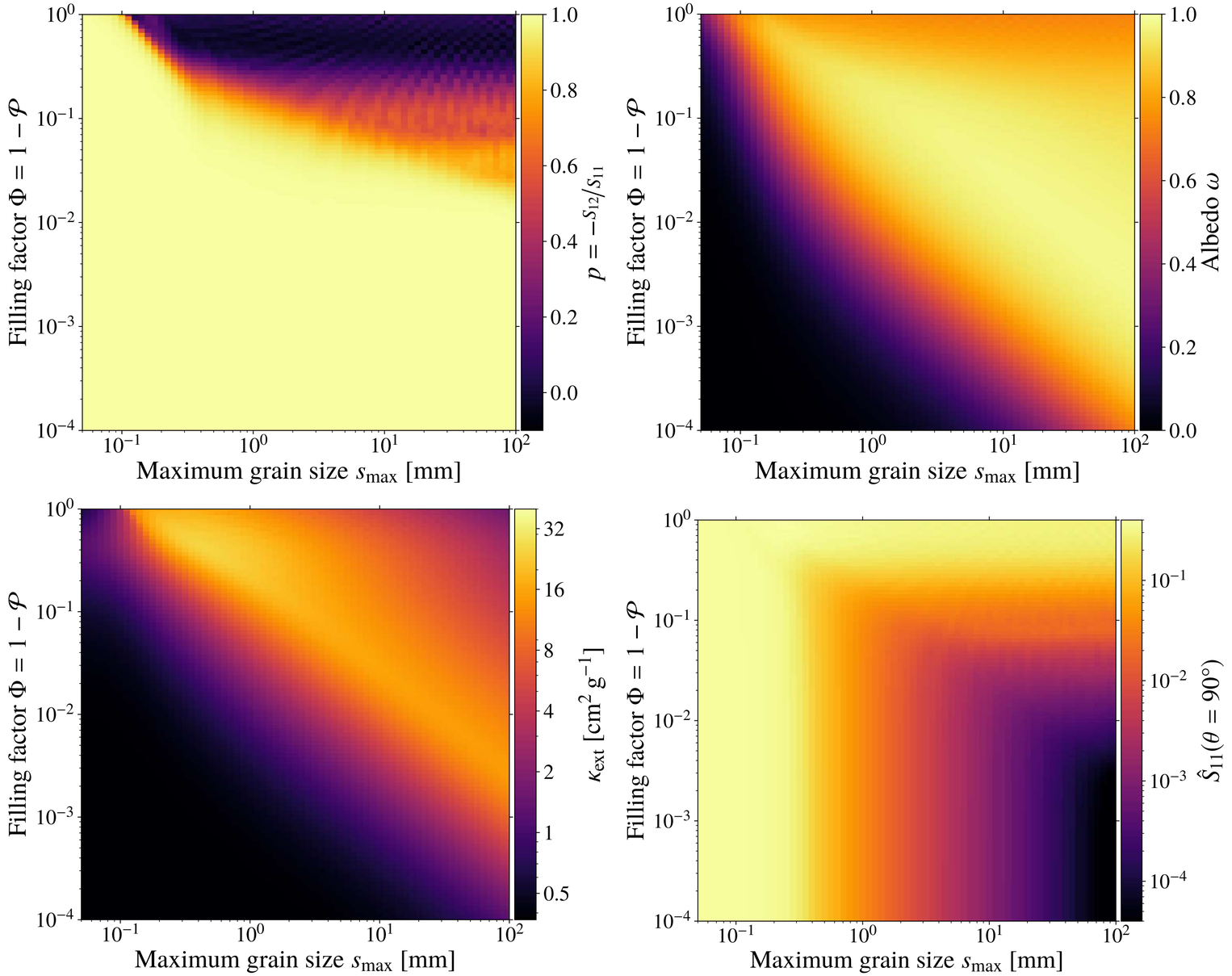

Fig. 1. Degree of polarisation for single scattering $p = -S_{12}/S_{11}$ for a scattering angle of $\theta = 90°$ *(upper left)*, albedo ω *(upper right)*, extinction opacity *(lower left)*, and probability density function $\hat{S}_{11}$ for the scattering angle $\theta = 90°$ *(lower right)*. All quantities are calculated for a grain size distribution with $q = -3.5$, $s_{\min} = 5$ nm and different upper grain size limits $s_{\max}$ at a wavelength of 850 µm for astrosil.

- 左上：１回散乱の偏光度。1だと偏光が100%。この数字が高いほど偏光が受かりやすい
- 右上：アルベド。散乱の効率。この数字が高いほど散乱しやすい。
- 左下：extinction opacity。そもそもの天体の明るさ。
- 右下：90度散乱の効率。この数字が低いと前方散乱→あんまりうれしくない

$$\frac{S_{11}(\theta)}{\int_0^\pi S_{11} \sin\theta \, \mathrm{d}\theta}$$

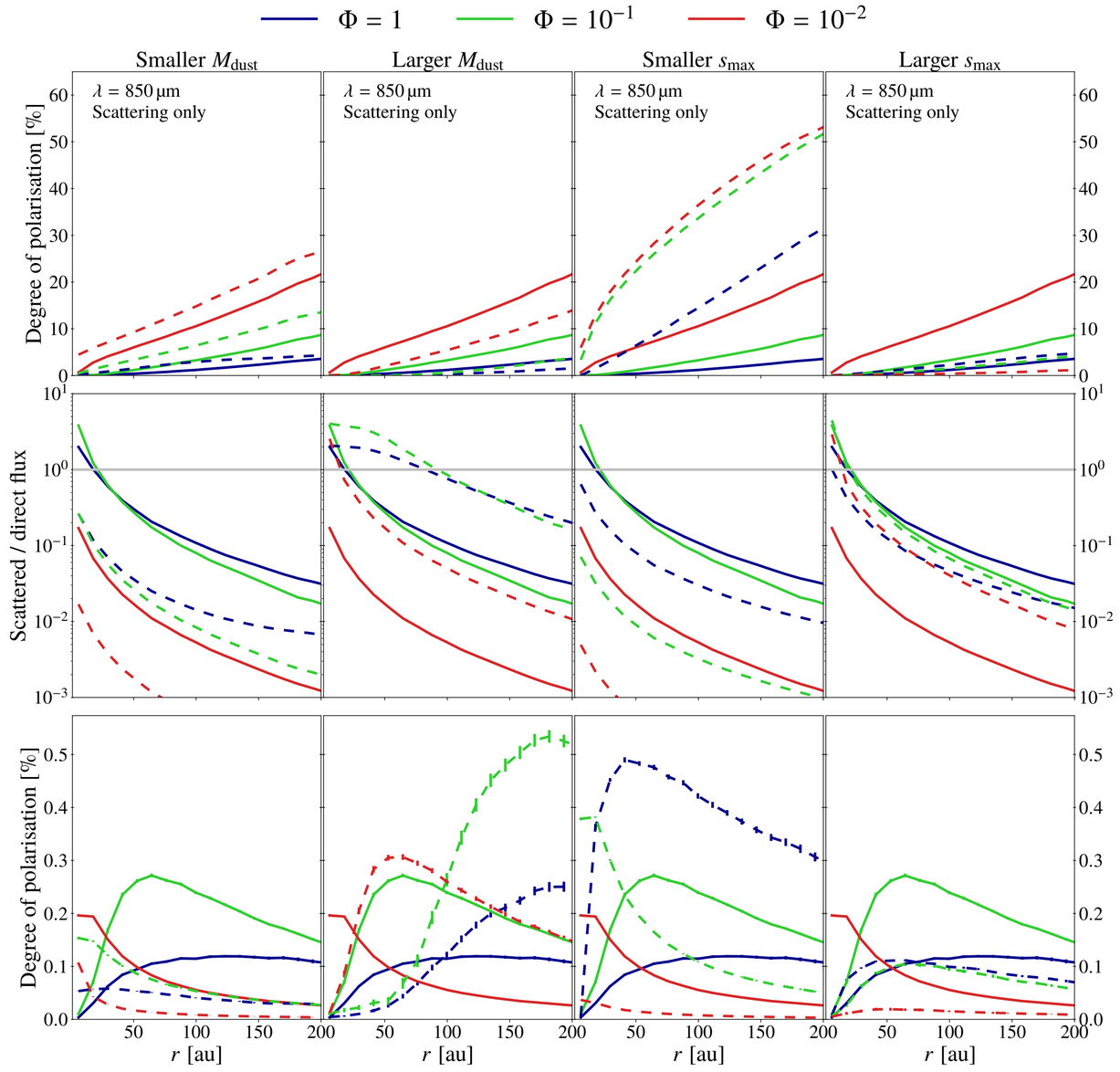

Fig. 3. Radial profiles of different quantities for disks with different filling factors (colours). The reference disk model (solid lines) is shown in a comparison with different disk models (dashed lines): A disk with a dust mass $M_{\rm dust} = 10^{-5}\,{\rm M}_\odot$ lower by a factor ten (*first column*), a disk with a dust mass $M_{\rm dust} = 10^{-3}\,{\rm M}_\odot$ higher by a factor ten (*second column*), a disk with a maximum grain size $s_{\rm max} = 100\,\mu{\rm m}$ smaller by a factor ten (*third column*), and a disk with a maximum grain size $s_{\rm max} = 10\,{\rm mm}$ larger by a factor ten (*fourth column*). *Top*: Degree of polarisation for scattering only, i.e. without the unpolarised direct re-emission. *Middle*: Flux ratio of scattered to direct re-emission. *Bottom*: Net degree of polarisation of the total flux, i.e. scattered and direct radiation, including vertical error bars.

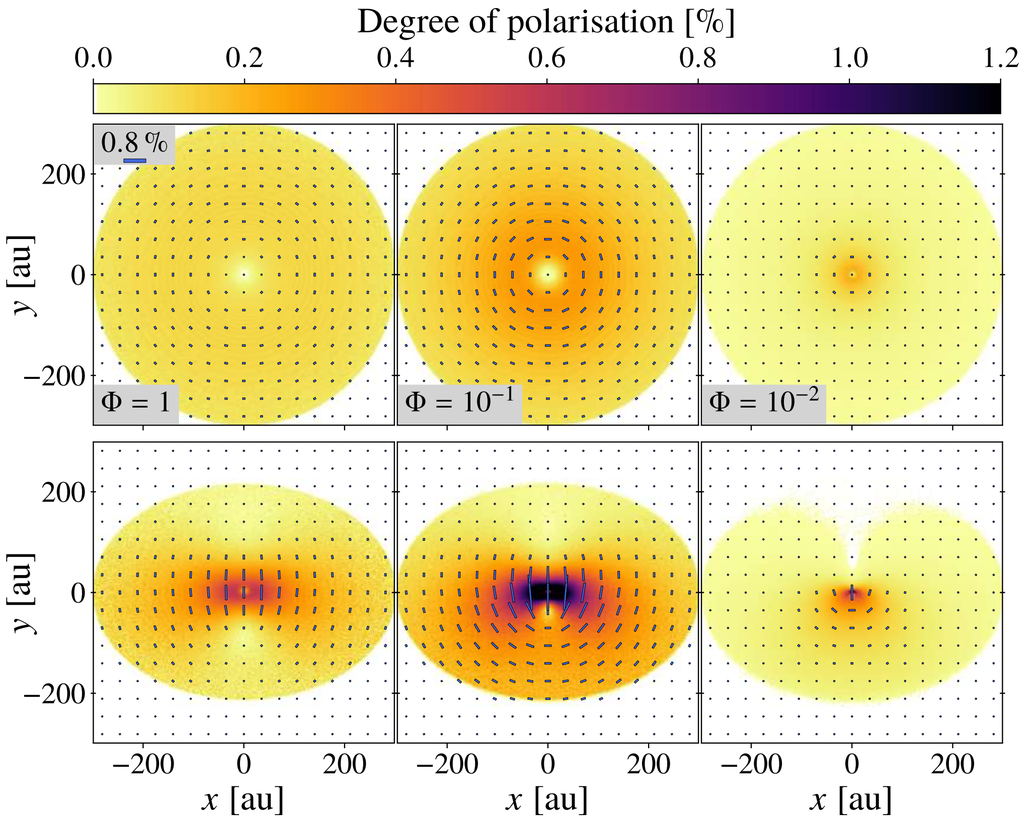

Fig. 7. Map of the polarisation degree with superimposed polarisatic vectors for our reference disk with $\Phi = 1$ (*left*), 10^{-1} (*centre*), and 10^{-} (*right*), and an inclination of $i = 0°$ (*top*) and 45° (*bottom*). The lengths the polarisation vectors are scaled to the polarisation degree, as indicate in the top left corner.

- **偏光度は高くても0.5%程度**
- **スペクトル指数は合わない**

ALMA-IRDC: Dense gas mass distribution from cloud to core scales

A. T. Barnes, J. D. Henshaw, F. Fontani, J. E. Pineda, G. Cosentino, J. C. Tan, P. Caselli, I. Jiménez-Serra, C. Y. Law, A. Avison, F. Bigiel, S. Feng, S. Kong, S. N. Longmore, L. Moser, R. J. Parker, Á. Sánchez-Monge, K. Wang

Infrared dark clouds (IRDCs) are potential hosts of the elusive early phases of high-mass star formation (HMSF). Here we conduct an in-depth analysis of the fragmentation properties of a sample of 10 IRDCs, which have been highlighted as some of the best candidates to study HMSF within the Milky Way. To do so, we have obtained a set of large mosaics covering these IRDCs with ALMA at band 3 (or 3mm). These observations have a high angular resolution (~3arcsec or ~0.05pc), and high continuum and spectral line sensitivity (~0.15mJy/beam and ~0.2K per 0.1km/s channel at the N2H+(1-0) transition). From the dust continuum emission, we identify 96 cores ranging from low- to high-mass (M = 3.4 to 50.9Msun) that are gravitationally bound (alpha_vir = 0.3 to 1.3) and which would require magnetic field strengths of B = 0.3 to 1.0mG to be in virial equilibrium. We combine these results with a homogenised catalogue of literature cores to recover the hierarchical structure within these clouds over four orders of magnitude in spatial scale (0.01pc to 10pc). Using supplementary observations at an even higher angular resolution, we find that the smallest fragments (<0.02pc) within this hierarchy do not currently have the mass and/or the density required to form high-mass stars. Nonetheless, the new ALMA observations presented in this paper have facilitated the identification of 19 (6 quiescent and 13 star-forming) cores that retain >16Msun without further fragmentation. These high-mass cores contain trans-sonic non-thermal motions, are kinematically sub-virial, and require moderate magnetic field strengths for support against collapse. The identification of these potential sites of high-mass star formation represents a key step in allowing us to test the predictions from high-mass star and cluster formation theories.

arXiv:2103.09122 **[astro-ph.GA]**

- 10個の赤外線暗黒星雲IRDCについて、ALMA 3 mm波で観測した。
- 空間分解能 3 arcsec = 0.05 pc
- ダスト連続波からは、96個のコアを見つけた。質量は3.4-50.9Msun
- alpha_vir = 0.3-1.3 (重力的に束縛されている)
- ビリアル平衡に達するためには、B=0.3-1.0 mGくらい必要
- 0.02 pc以下のフラグメントは、その質量が大質量星を作れないほど小さかった。
- だが、それでも19のコアが（16Msun以上）同定された

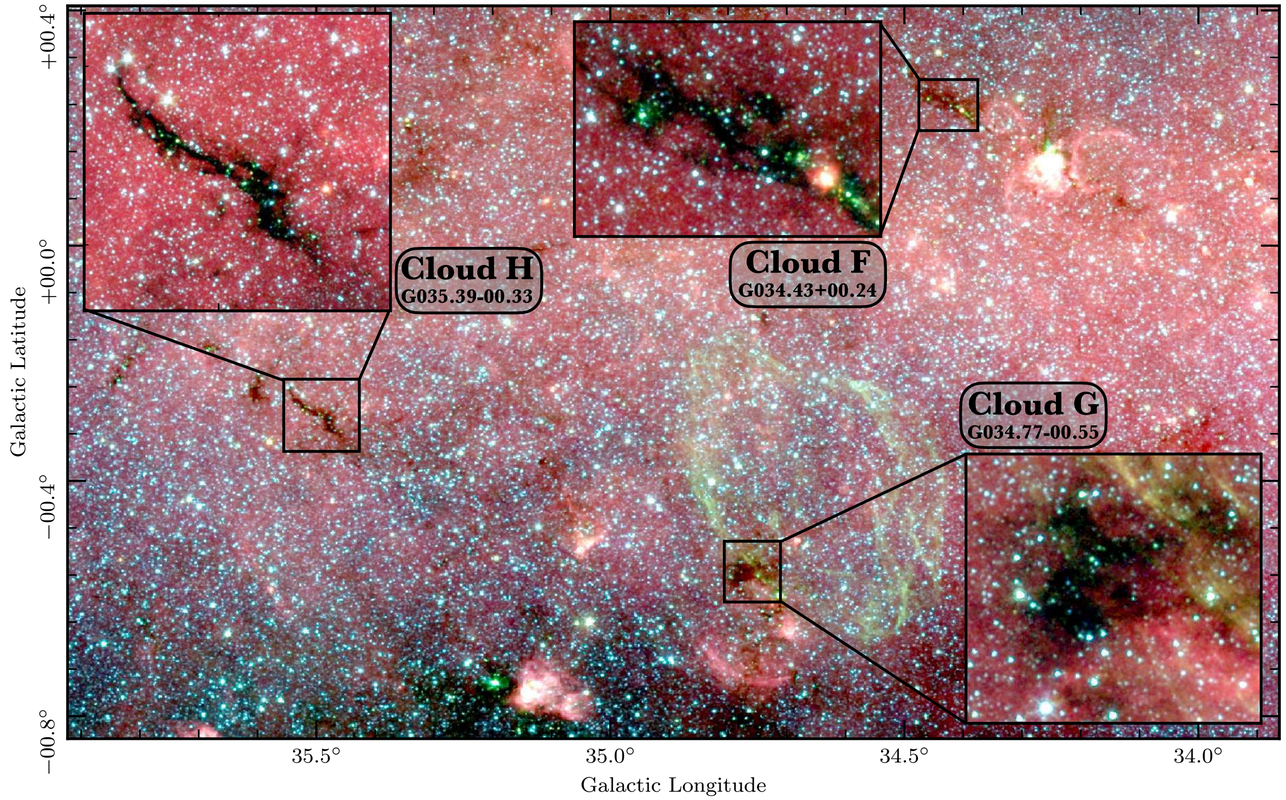

Figure 1. A three colour image of the Galactic plane where several infrared dark clouds (IRDCs) can be seen as dark extinction features. In this image, red is 8 µm, green is 5.8 µm and blue is 4.5 µm emission from the *Spitzer* GLIMPSE survey (Carey et al. 2009). Labelled are three IRDCs that are investigated within this work: Clouds F, G and H (or G034.43+00.24, G034.77-00.55, G035.39-00.33). The panels show zoom-ins of these IRDCs for more detail.

Cloud	ID "G(longitude)(latitude)"	v_{sys} km s^{-1}	D_{cl} pc	$R_{eff,cl}$ pc	M_{cl} M$_\odot$	σ_{cl} km s^{-1}	$\alpha_{vir,cl}$ -	$T_{dust,cl}$ K	$\sigma_{NT,cl}$ km s^{-1}	$\mathcal{M}_{NT,cl}$ -	n_c #
Cloud A	G018.82-00.28	59-69	4800	10.4	18500.0	2.04	1.4	18.3	2.0	7.9	8
Cloud B	G019.27+00.07	22-32	2400	2.71	2200.0	1.6	2.2	17.8	1.6	6.3	10
Cloud C	G028.37+00.07	73-83	5000	15.4	53200.0	3.72	2.4	17.7	3.7	14.8	16
Cloud D	G028.53-00.25	81-91	5700	16.9	74300.0	1.85	0.5	16.9	1.8	7.5	16
Cloud E	G028.67+00.13	75-85	5100	11.5	28700.0	4.32	1.1	19.1	4.3	16.5	4
Cloud F	G034.43+00.24	52-62	3700.0	3.5	4460.0	3.62	1.3	20.0	3.6	13.5	20
Cloud G	G034.77-00.55	35-45	2900	3.06	3300.0	3.28	4.7	19.8	3.3	12.3	0
Cloud H	G035.39-00.33	38-48	2900	9.69	16700.0	2.03	0.7	19.5	2.0	7.6	10
Cloud I	G038.95-00.47	38-48	2700	3.73	2700.0	1.65	1.2	18.0	1.6	6.4	9
Cloud J	G053.11+00.05	17-27	1800	0.755	200.0	0.96	1.5	19.0	0.9	3.5	3

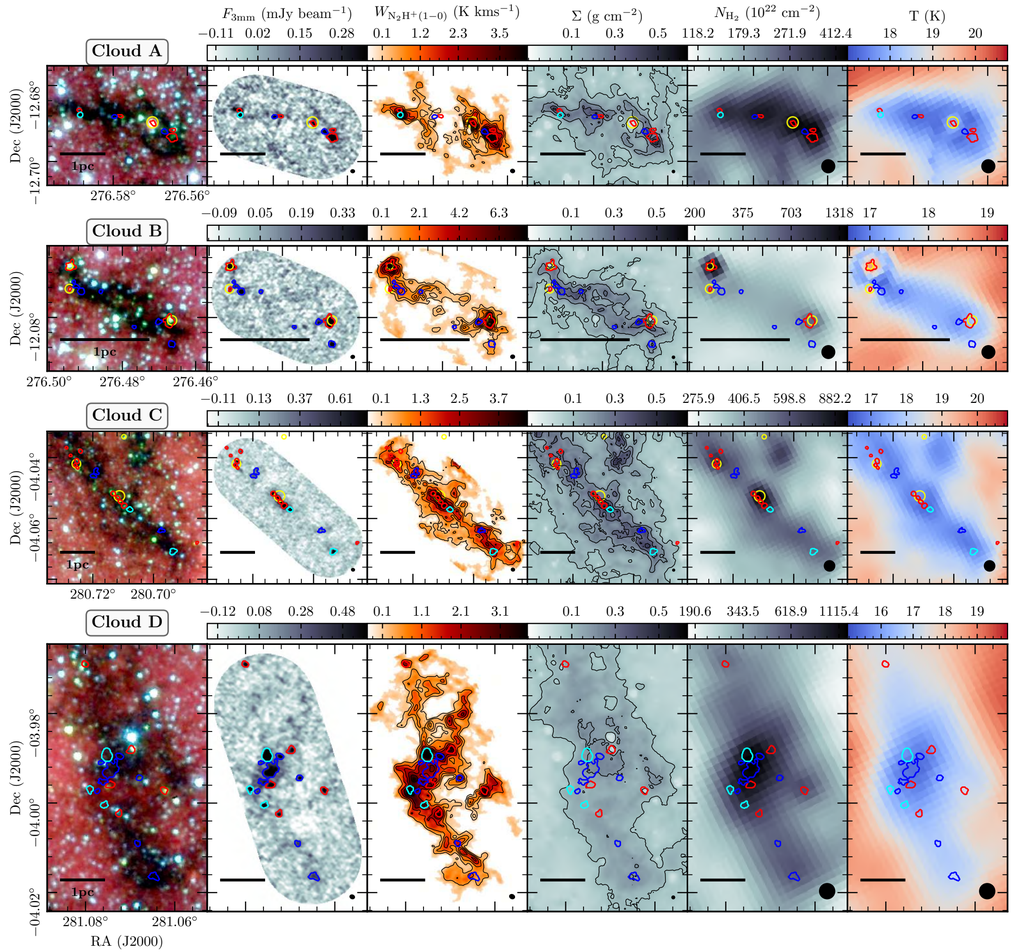

Figure 2. (first column) Three colour images from the *Spitzer* GLIMPSE survey (Churchwell et al. 2009). (second) The ALMA 3 mm dust continuum (without the primary beam correction), and (third) N_2H^+ (J,F_1,F = 1,0,1 → 0,1,2) integrated intensity maps. (fourth) Combined near- and mid-infrared extinction derived mass surface density maps (Kainulainen & Tan 2013). (fifth) Far-infrared *Herschel* derived column density, and (sixth) dust temperature maps (Marsh et al. 2016, 2017). The yellow circles overlaid on each panel show the positions and sizes of 70 µm emission point sources (Molinari et al. 2016; Marton et al. 2017). The coloured contours overlaid on each panel show boundaries of all the "leaves" (or cores) identified using the dendrogram analysis on the dust continuum maps (see section 3.1). The red and blue contours indicate the cores that have been classified as star-forming and quiescent, respectively (section 3.1). The cyan contours indicate the cores that have been identified as being quiescent, high-mass and without further fragmentation (see section 4.3.2). Shown in the lower left of the ALMA observation panels is the beam size, and in the lower left of the three colour image (first panel) is a scale bar adjusted for the distance of each cloud (see Table 1).

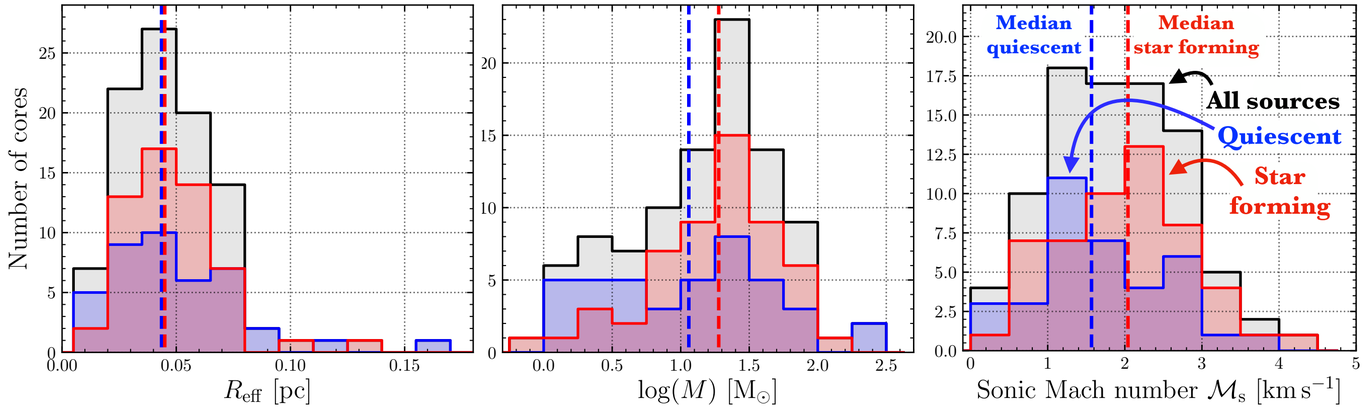

Figure 3. Distribution of the properties determined across the core sample (section 3.3). Shown in panels from left to right is the effective radius ($R_{\rm eff}$), the (logarithm) mass (M), and sonic Mach number ($\mathcal{M}_{\rm s} = \sigma_{\rm NT}/\sigma_{\rm T}$) calculated across the core sample (section 3.3). Shown as black, red and blue stepped profiles are histograms for the whole sample, the star-forming cores and quiescent (non-star forming) cores, respectively. The red and blue vertical dashed lines show the median values for the star-forming cores and quiescent cores.

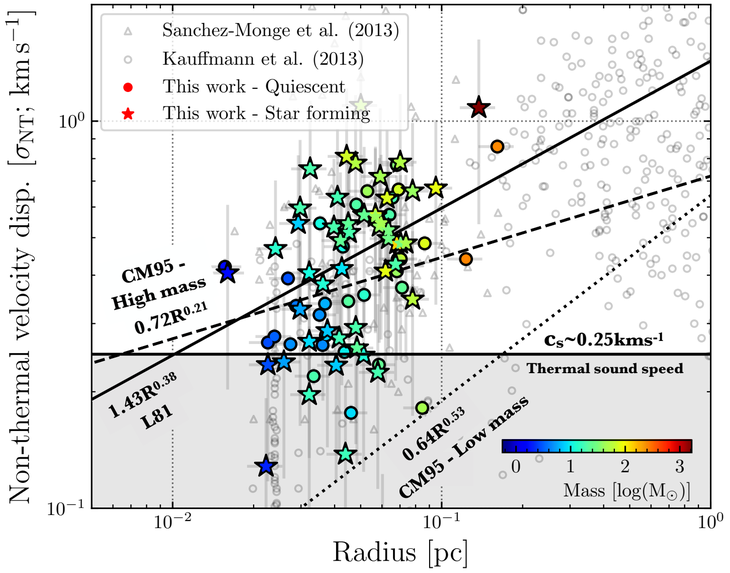

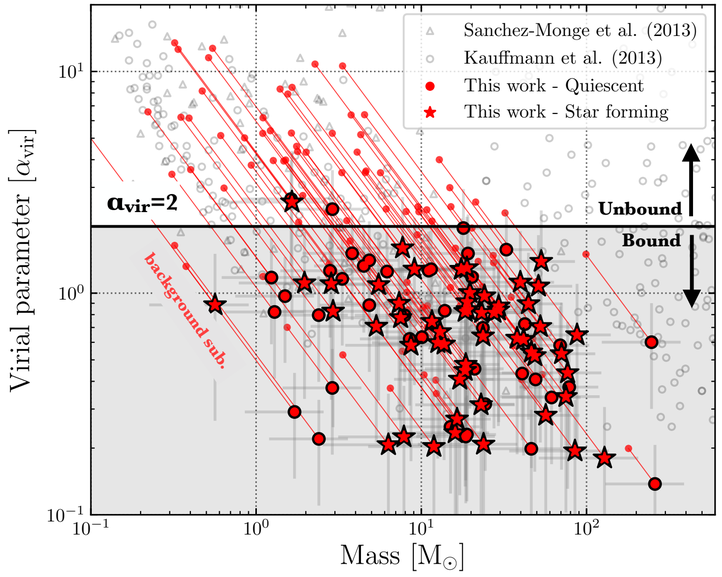

- 10個の赤外線暗黒星雲IRDCについて、ALMA 3 mm波で観測した。
- ダスト連続波からは、96個のコアを見つけた。質量は3.4-50.9Msun
- 速度はN2H+を使って求めた
- Ms = 0.9 – 2.7, and virial parameters of αvir = 0.3 – 1.3
-

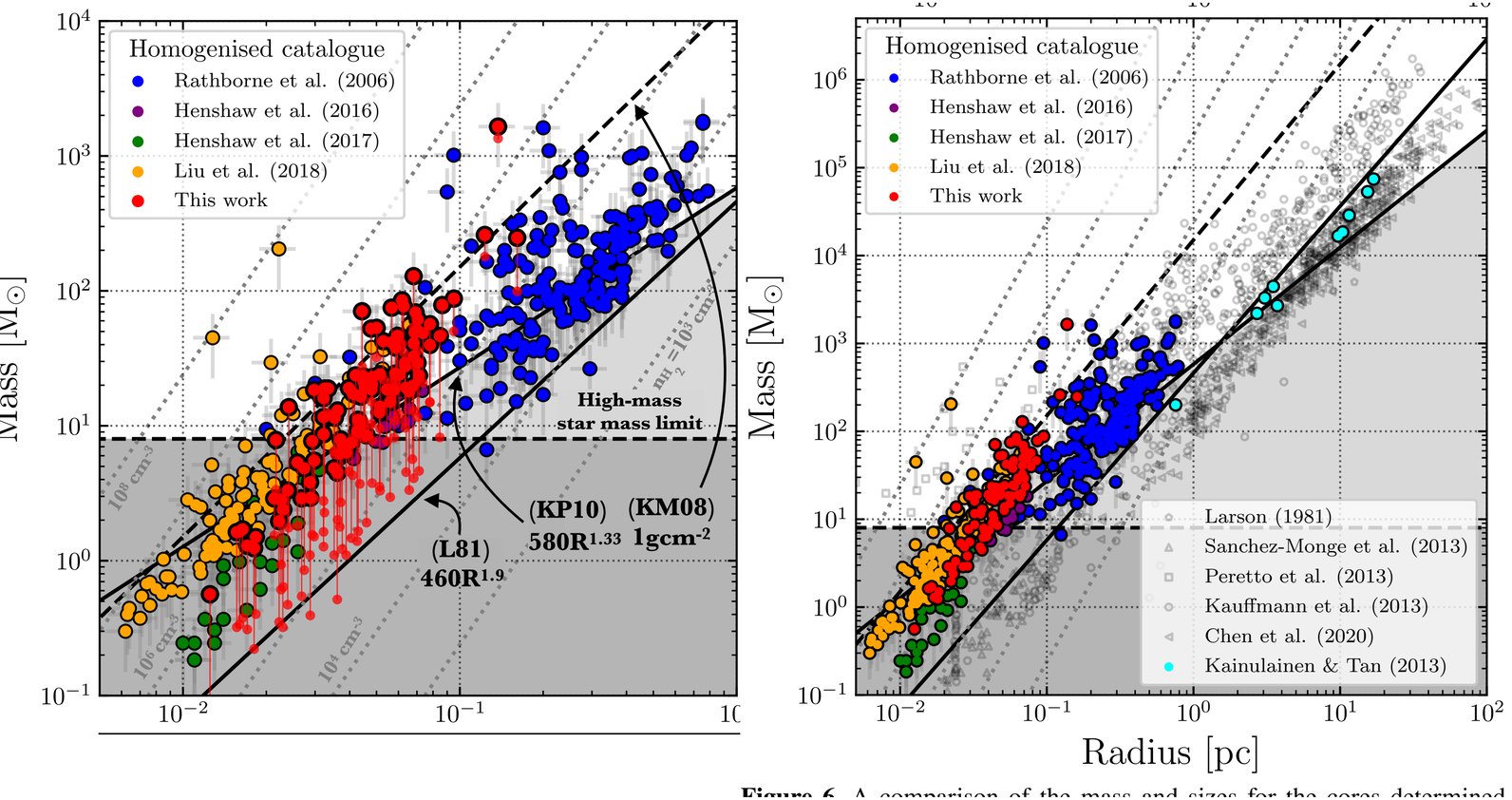

Figure 6. A comparison of the mass and sizes for the cores determined in this work, to samples taken from the literature, and mass-size relations and thresholds for massive star formation. Shown as black-outlined red points are the cores studied in this work (M), which are connected to their corresponding lower background-subtracted masses ($M^{\rm b}$; see Table A2). Highlighted as coloured points are the mass and sizes of the cores and/or clumps determined by Liu et al. (2018b), Henshaw et al. (2016a), Henshaw et al. (2017), and Rathborne et al. (2006), which have crossover with the IRDC sample examined in this work. The properties of these cores have been recalculated using the same assumptions outlined in this work (section 4.1). (lower panel) Shown as grey open points are the properties taken directly from Larson (1981), Kauffmann et al. (2013), Peretto et al. (2013), Sánchez-Monge et al. (2013), and Chen et al. (2020). Overlaid as diagonal solid black lines are the mass-radius relations taken from Larson (1981, L81), and high-mass star formation thresholds taken from Krumholz & McKee (2008, KM08) and Kauffmann & Pillai (2010, KP10). The KP10 relation has been scaled by a factor of 1.5 to match the dust opacity used throughout this paper. The horizontal dotted black line shows the mass threshold of high-mass stars (>8 $M_\odot$). The dashed diagonal grey lines show constant number densities (as labelled).

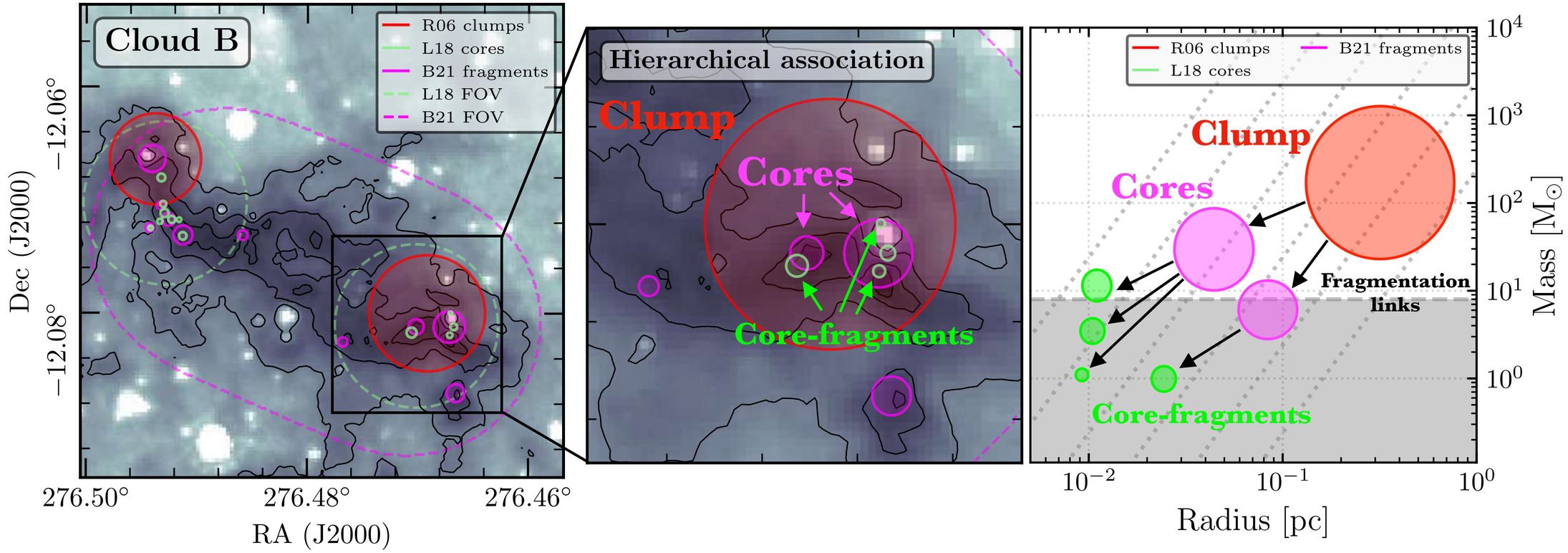

Figure 8. A schematic diagram showing the fragmentation linking procedure, which we use to determine a hierarchy of structures similar to a dendrogram across multiple datasets covering our cloud sample (section 4.3). The left panel shows the near- and mid-infrared extinction derived mass surface density map for Cloud B in greyscale, overlaid with circles representing the position and sizes of the cores contained within the homogenised catalogue (section 4.1). The red circles show the Rathborne et al. (2006, R06) clumps, the solid magenta circles show the cores identified in this work (B21), and the solid green circles show the core-fragments identified by Liu et al. (2018b, L18). The dashed magenta and green lines show the field of view (FOV) of the ALMA observations presented in this work and in L18, respectively. The centre panel shows a zoom-in of the MM2 R06 core within Cloud B, which is highlighted on the left panel by a solid black box. Here the clump, core and core-fragment structures have been labelled. The right panel shows the mass as a function of radius for the example MM2 region. Here we show the fragmentation links between the host clump, and the cores and core fragments contained within its boundary.

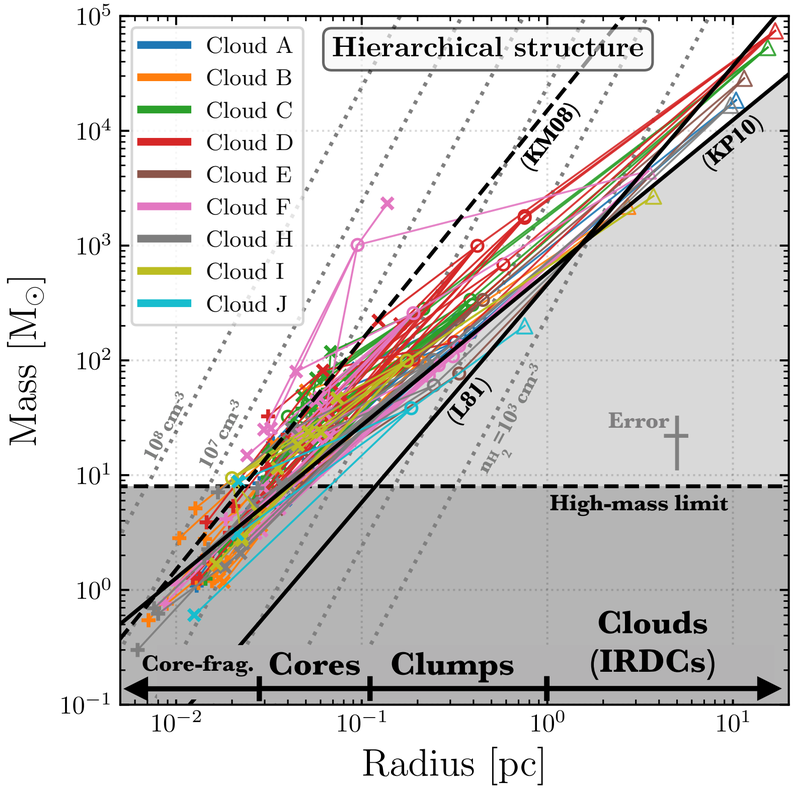

Figure 9. The clump-to-core fragment masses within each cloud as a function of the size-scale. The circles, crosses and plus sign markers represent the clumps from R06, cores from this work and the clumps from L18. The straight lines connect the symbols for each core/core-fragment to the larger, host clump/core and then cloud (see Figure A1 in the appendix for all clouds plotted separately). The lines and symbols have been coloured by cloud as indicated in the legend located in the upper left. The dotted diagonal grey lines show constant number densities (as labelled), and the black lines show the high-mass star formation thresholds shown in Figure 6. In the lower right, we show a representative uncertainty range ∼15 and ∼50 per cent on the radius and mass, respectively.

過去文献から同じエリアのデータを引っ張ってきて合わせて再解析した。その結果、質量-半径のプロットをしてみると、the cloud (~10 pc) to clump (~0.5 pc), and to the core (<0.1 pc) scales のスケールであまりシンプルなパワーローには乗っていなかった。

- **小さいコアに着目。< 0.02 pc (~2000 au) 以下では大質量星を作れない。**
- **ここからhierarchical structure を使って、質量は星を作るほど大きいが、これ以上fragmentしない天体１９個を同定した。**
- **そのうち１３個は星形成の兆候あり。残り６個はいい候補か。**
- **マッハ数の中間値2.4くらいのtranssonic**
- **kinematically subvirial (medianα =0.5)**
- **なので、支えるには磁場が必要（median B of 930 μ G)**

Particle acceleration and magnetic field amplification in massive young stellar object jets

Anabella Araudo, Marco Padovani, Alexandre Marcowith

Synchrotron radio emission from non-relativistic jets powered by massive protostars has been reported, indicating the presence of relativistic electrons and magnetic fields of strength ~0.3-5 mG. We study diffusive shock acceleration and magnetic field amplification in protostellar jets with speeds between 300 and 1500 km/s. We show that the magnetic field in the synchrotron emitter can be amplified by the non-resonant hybrid (Bell) instability excited by the cosmic-ray streaming. By combining the synchrotron data with basic theory of Bell instability we estimate the magnetic field in the synchrotron emitter and the maximum energy of protons. Protons can achieve maximum energies in the range 0.04-0.65 TeV and emit gamma rays in their interaction with matter fields. We predict detectable levels of gamma rays in IRAS 16547-5247 and IRAS 16848-4603. The gamma ray flux can be significantly enhanced by the gas mixing due to Rayleigh-Taylor instability. The detection of this radiation by the Fermi satellite in the GeV domain and the forthcoming Cherenkov Telescope Array at higher energies may open a new window to study the formation of massive stars, as well as diffusive acceleration and magnetic field amplification in shocks with velocities of about 1000 km/s.

Comments:
17 pages, 8 figures. Accepted for publication in MNRAS
arXiv:2102.11583 **[astro-ph.HE]**

- 大質量星からの非相対論的ジェットから、シンクロトロン電波放射が報告されている。
- diffusive shock accelerationと原子星ジェットにおける磁場による増幅でこれが再現されるか検討してみた

- non-resonant hybrid (Bell) instabilityによって磁場が増幅される。
- シンクロトロン放射体のプロトンは0.04-0.65TeVに達する。
- IRAS 16547-5247 と IRAS 16848-4603からはガンマ線が検出可能であることを予言する

A VLA Census of the Galactic H II Region Population

William P. Armentrout, Loren D. Anderson, Trey V. Wenger, Dana S. Balser, Thomas M. Bania

The Milky Way contains thousands of H II region candidates identified by their characteristic mid-infrared morphology, but lacking detections of ionized gas tracers such as radio continuum or radio recombination line emission. These targets thus remain unconfirmed as H II regions. With only ~2500 confirmed H II regions in the Milky Way, Galactic surveys are deficient by several thousand nebulae when compared to external galaxies with similar star formation rates. Using sensitive 9 GHz radio continuum observations with the Karl G. Jansky Very Large Array (VLA), we explore a sample of H II region candidates in order to set observational limits on the actual total population of Galactic H II regions. We target all infrared-identified "radio quiet" sources from the WISE Catalog of Galactic H II regions between $245^\circ \geq \ell \geq 90^\circ$ with infrared diameters less than 80''. We detect radio continuum emission from 50% of the targeted H II region candidates, providing strong evidence that most of the radio quiet candidates are bona fide HII regions. We measure the peak and integrated radio flux densities and compare the inferred Lyman continuum fluxes using models of OB-stars. We conclude that stars of approximately spectral type B2 and earlier are able to create H II regions with similar infrared and radio continuum morphologies as the more luminous H II regions created by O-stars. From our 50% detection rate of "radio quiet" sources, we set a lower limit of ~7000 for the H II region population of the Galaxy. Thus the vast majority of the Milky Way's H II regions remain to be discovered.

Comments:
11 pages of text, 146 infrared/radio images of faint HII region candidates
(or arXiv:2103.02049v1 **[astro-ph.GA]** for this version)

- 銀河系においてHII領域の候補は、 中間赤外で発見されている。だが、電波源や再結合線が見えずにHII領域と特定されていないものが多い。
- VLAを使って、9GHzの電波連続波のHII領域候補を調べた。
- WISE(赤外)で同定されたが、電波で見えていない天体を全部見た。
- 結果、50%の天体から電波を受けた。
- 星のモデルと比較した結果、B2かそれより早い星ならHII領域を作れることがわかった。
- 50%の検出率から、少なくとも銀河系には7000のHII領域があると見積もった。これは、これまで確認された2500に対して、まだまだ見つかっていない領域がたくさんあることを示している。

Fragmentation in the massive G31.41+0.31 protocluster

M. T. Beltrán, V. M. Rivilla, R. Cesaroni, L. T. Maud, D. Galli, L. Moscadelli, A. Lorenzani, A. Ahmadi, H. Beuther, T. Csengeri, S. Etoka, C. Goddi, P. D. Klaassen, R. Kuiper, M. S. N. Kumar, T. Peters, Á. Sánchez-Monge, P. Schilke, F. van der Tak, S. Vig, H. Zinnecker

Context. ALMA observations at 1.4 mm and 0.2" (750au) angular resolution of the Main core in the high-mass star forming region G31.41+0.31 have revealed a puzzling scenario: on the one hand, the continuum emission looks very homogeneous and the core appears to undergo solid-body rotation, suggesting a monolithic core stabilized by the magnetic field; on the other hand, rotation and infall speed up toward the core center, where two massive embedded free-free continuum sources have been detected, pointing to an unstable core having undergone fragmentation. Aims. To establish whether the Main core is indeed monolithic or its homogeneous appearance is due to a combination of large dust opacity and low angular resolution, we carried out millimeter observations at higher angular resolution and different wavelengths. Methods. We carried out ALMA observations at 1.4 mm and 3.5 mm that achieved angular resolutions of 0.1"(375 au) and 0.075" (280 au), respectively. VLA observations at 7 mm and 1.3 cm at even higher angular resolution, 0.05" (190 au) and 0.07" (260 au), respectively, were also carried out to better study the nature of the free-free continuum sources detected in the core. Results. The millimeter continuum emission of the Main core has been clearly resolved into at least four sources, A, B, C, and D, within 1", indicating that the core is not monolithic. The deconvolved radii of the dust emission of the sources, estimated at 3.5 mm, are 400-500au, their masses range from 15 to 26 Msun, and their number densities are several 1E9 cm-3. Sources A and B, located closer to the center of the core and separated by 750 au, are clearly associated with two free-free continuum sources, likely thermal radio jets, and are the brightest in the core. The spectral energy distribution of these two sources and their masses and sizes are similar and suggest a common origin.

arXiv:2103.04953 [astro-ph.GA]

- 大質量原始星G31.41+0.31という天体を高分解能ALMA観測したら、よく分解して見れた→単体ではない。

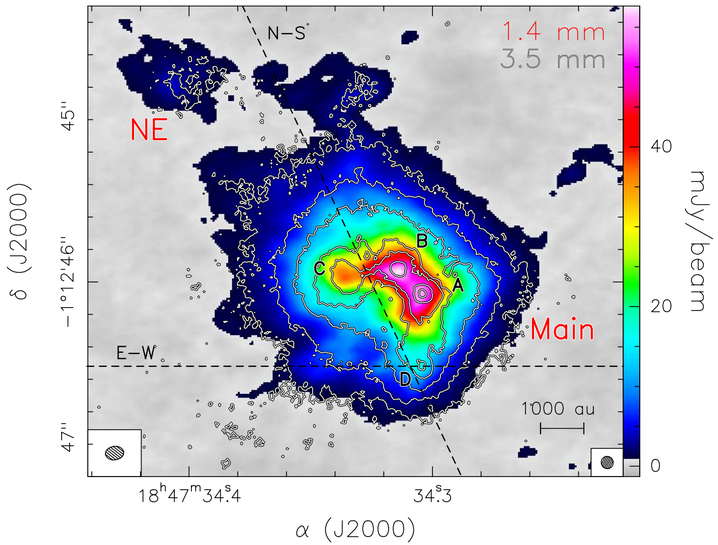

Fig. 2. Overlay of the ALMA 3.5 mm continuum emission (*white contours*) on the 1.4 mm continuum emission (*colors*) toward cores *NE* and *Main* in G31. The white contours are 3, 6, 10, 15, 20, 30, and 40 times 1σ, which is 0.16 mJy beam^{-1}. The 1.4 mm and 3.5 mm synthesized beams are shown in the lower left-hand and right-hand corner, respectively. The names of the sources in which the emission of the *Main* core has been resolved (see Sect. 3.1 and Table 2) are indicated. Dashed black lines indicate the direction of the E–W and N–S outflows mapped in SiO by B18.

Fitting an Analytic Magnetic Field to a Prestellar Core

Gianfranco Bino, Shantanu Basu

We deploy and demonstrate the capabilities of the magnetic field model developed by Ewertowski & Basu (2013) by fitting observed polarimetry data of the prestellar core FeSt 1-457. The analytic hourglass magnetic field function derived directly from Maxwell's equations yields a central-to-surface magnetic field strength ratio in the equatorial plane, as well as magnetic field directions with relative magnitudes throughout the core. This fit emerges from a comparison of a single plane of the model with the polarization map that results from the integrated properties of the magnetic field and dust throughout the core. Importantly, our fit is independent of any assumed density profile of the core. We check the robustness of the fit by using the POLARIS code to create synthetic polarization maps that result from the integrated scattering and emission properties of the dust grains and their radiative transfer, employing an observationally-motivated density profile. We find that the synthetic polarization maps obtained from the model also provides a good fit to the observed polarimetry. Our model fits the striking feature of significant curvature of magnetic field lines in the outer part of FeSt 1-457. Combined with independent column density estimates, we infer that the core of size Rgas has a mildly supercritical mass-to-flux ratio and may have formed through dynamical motions starting from a significantly larger radius R. A breakdown of flux-freezing through neutral-ion slip (ambipolar diffusion) could be responsible for effecting such a transition from a large-scale magnetic field structure to a more compact gas structure.

arXiv:2103.03324 **[astro-ph.SR]**

- 原始星コアの偏光データをフィッティングするための公式を作ってみた
- この公式は密度プロファイルによらない。
- 輻射輸送を使って確認した。
- FeSt 1-457という天体にも応用した
- このコアはサブクリティカル

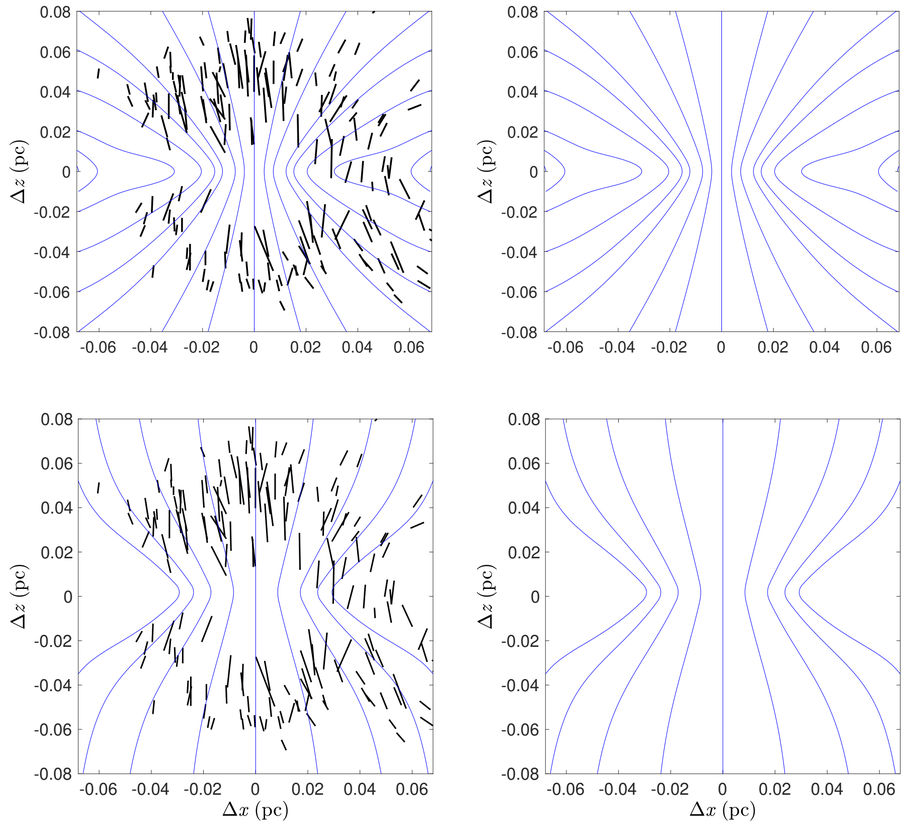

Figure 2. Model magnetic field fits with a line spacing not indicative of the field strength. Top: Model with $R = 0.1$ pc. Bottom: Model with $R = 0.2$ pc. model is shown in the region where there are observed polarization segments, overlaid with polarization segments on the left, and without polarization segr on the right.

Magnetic fields and Star Formation around HII regions: The S235 complex

R. Devaraj, D. P. Clemens, L. K. Dewangan, A. Luna, T. P. Ray, J. Mackey

Magnetic fields are ubiquitous and essential in star formation. In particular, their role in regulating formation of stars across diverse environments like HII regions needs to be well understood. In this study, we present magnetic field properties towards the S235 complex using near-infrared (NIR) H-band polarimetric observations, obtained with the Mimir and POLICAN instruments. We selected 375 background stars in the field through combination of Gaia distances and extinctions from NIR colors. The plane-of-sky (POS) magnetic field orientations inferred from starlight polarization angles reveal a curved morphology tracing the spherical shell of the HII region. The large-scale magnetic field traced by Planck is parallel to the Galactic plane. We identified 11 dense clumps using 1.1mm dust emission, with masses between 33−525M⊙. The clump averaged POS magnetic field strengths were estimated to be between 36−121μG, with a mean of ~65μG. The mass-to-flux ratios for the clumps are found to be sub-critical with turbulent Alfvén Mach numbers less than 1, indicating a strongly magnetized region. The clumps show scaling of magnetic field strength vs density with a power-law index of 0.52 ± 0.07, similar to ambipolar diffusion models. Our results indicate the S235 complex is a region where stellar feedback triggers new stars and the magnetic fields regulate the rate of new star formation.

arXiv:2103.02956 **[astro-ph.GA]**

- S235のNIR偏光結果
- 375の背景星を利用
- HII領域を沿うような磁場構造を発見

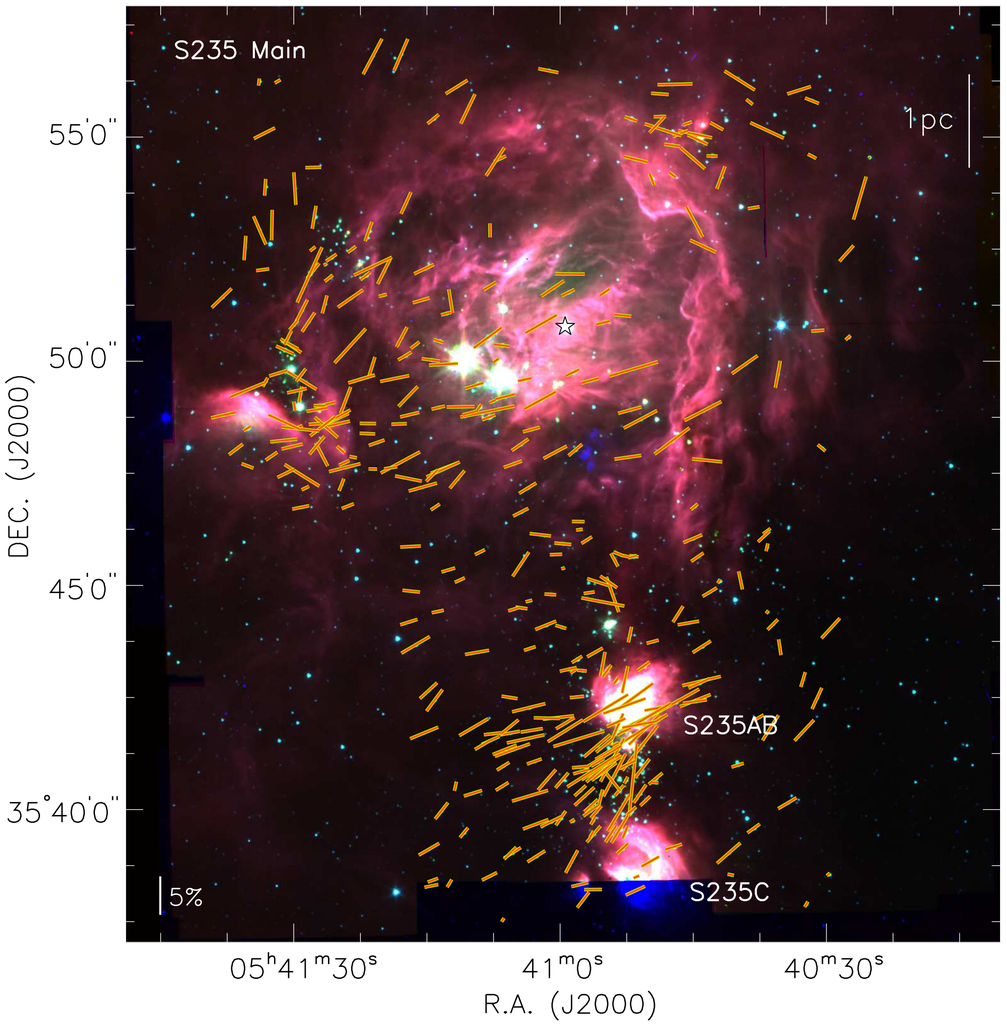

Figure 8. Magnetic field morphology in the S235 complex. The background image is the same *Spitzer* IRAC composite map shown in Figure 1. The NIR background starlight polarizations are indicated by red-yellow ps The lengths of the vectors indicate the polarization percentages and a reference vector length is shown at the bott

Water in star-forming regions (WISH): Physics and chemistry from clouds to disks as probed by Herschel spectroscopy

E.F. van Dishoeck (Leiden), L.E. Kristensen (Copenhagen), the WISH team (50 co-authors)

(abridged) Data and results from the WISH key program are summarized, designed to provide a legacy data set to address its physics and chemistry. WISH targeted ~80 sources along the two axes of luminosity and evolutionary stage: from low- to high-mass protostars and from pre-stellar cores to protoplanetary disks. Lines of H2O, HDO, OH, CO and [O I] were observed with the HIFI and PACS instruments, complemented by molecules that probe UV, X-ray or grain chemistry. Most of the far-infrared water emission from protostars is found to be compact, originating from warm outflowing and shocked gas at high density and temperature in at least two physical components. This gas is not probed by low-J CO lines, only by J>14. Water is a significant, but not dominant, coolant. Its abundance is universally low, of order H2O/H2=2E-6, pointing to shock and outflow cavity models that include UV radiation at 100-1000 times the ISRF. In cold quiescent pre-stellar cores and envelopes, the water abundance structure is accurately probed through velocity-resolved line profiles, confirming basic chemistry networks. The gaseous HDO/H2O ratio of 0.025, much higher than that of bulk ice, is representative of the outer photodesorbed ice layers and cold chemistry. Water abundances in the inner hot cores are high, but with variations from 5E-6 to 2E-4. Combined analyses of water gas and ice show that up to 50% of the oxygen budget may be missing, with possible explanations discussed. Water vapor emission from disks is weak, indicating that water ice is locked up in larger pebbles early on and that these pebbles have settled and drifted inward by the Class II stage. Quantitatively, many oceans of water ice are available. Extragalactic low-J H2O emission is mostly compact and collisionally excited. Prospects for future mid- to far-infrared missions are given.

arXiv:2102.02225 **[astro-ph.GA]**

- WISHのサマリー論文。
- ハーシェルを使って、80天体を観測
- 殆どの場合、遠赤外の水の輝線は、コンパクトで、温かいショックを経験したガスから。
- J>14のCO輝線でのみ検出される。
- 水は冷却輝線だが、支配的では似。